Published for SISSA by Springer

Received: January 16, 2023
Revised: March 21, 2023
Accepted: March 24, 2023
Published: March 31, 2023

Flavonstrahlung in the $B_3 - L_2$ Z' model at current and future colliders

Ben Allanach[a,b] **and Eetu Loisa**[a,*]

[a] *DAMTP, University of Cambridge, Wilberforce Road, Cambridge, CB3 0WA, United Kingdom*
[b] *Department of Theoretical Physics, CERN, 1211 Geneva 23, Switzerland*

E-mail: B.C.Allanach@damtp.cam.ac.uk, eal47@cam.ac.uk

Abstract: The $B_3 - L_2$ Z' model may explain some gross features of the fermion mass spectrum as well as $b \to s\ell\ell$ anomalies. A TeV-scale physical scalar field associated with gauged $U(1)_{B_3-L_2}$ spontaneous symmetry breaking, the flavon field ϑ, affects Higgs phenomenology via mixing. In this paper, we investigate the collider phenomenology of the flavon field. Higgs and W boson mass data are used to place bounds upon parameter space. We then examine *flavonstrahlung* ($Z' \to Z'\vartheta$ production) at colliders as a means to directly produce and discover flavon particles, which would provide direct empirical evidence tying the flavon to $U(1)_{B_3-L_2}$ symmetry breaking. A 100 TeV FCC-hh or a 10 TeV muon collider would have high sensitivity to flavonstrahlung, whereas the HL-LHC can observe it only in extreme corners of parameter space.

Keywords: Higgs Properties, Specific BSM Phenomenology

ArXiv ePrint: 2212.07440

*Corresponding author.

https://doi.org/10.1007/JHEP03(2023)253

JHEP03(2023)253

Contents

JHEP03(2023)253

1 Introduction

The $B_3 - L_2$ model [1–3] may be motivated by providing an explanation of some features of the fermion mass spectrum. It was originally introduced to explain discrepancies between Standard Model (SM) predictions and experimental measurements of various observable quantities that involve the $b \to s\mu^+\mu^-$ or $\bar{b} \to \bar{s}\mu^+\mu^-$ transition [4–13].[1] Whilst four of these measurements (two different q^2 bins each of R_K and R_{K^*}) have recently returned [16, 17] to being compatible with SM predictions, a larger number of other observables are in tension with them. A Z' contribution to the $b \to s\mu^+\mu^-$ process is depicted in the left-hand panel of figure 1. The $B_3 - L_2$ model is based on an extension of the SM gauge group by a direct product with an additional spontaneously broken $U(1)_{B_3-L_2}$ gauge symmetry, where the charges of the SM fields are proportional to third family baryon number minus

[1] Discrepancies between predictions and data are still present when one uses ratios of observables to cancel the dependence upon CKM matrix elements, whose determination from data is based on $\Delta M_{s,d}$, ϵ_K and $S_{\psi K_S}$ for which we find new physics contributions that are negligible [14, 15].

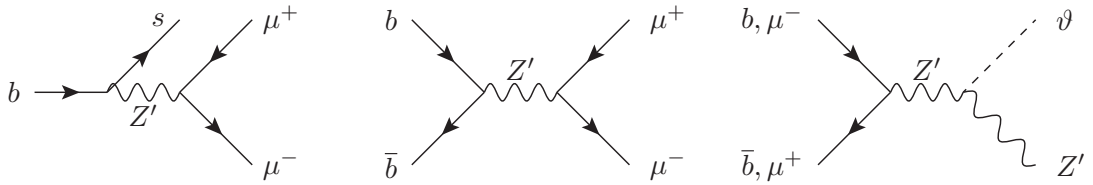

Figure 1. Feynman diagram of (left panel) Z' mediated contribution to $b \to s\mu^+\mu^-$, (middle panel) the dominant LHC Z' production process, followed by subsequent decay into a di-muon pair $\mu^+\mu^-$ and (right panel) flavonstrahlung at a hadron collider [$b\bar{b}$ initial state] or a muon collider [$\mu^+\mu^-$ initial state].

second family lepton number. The model is free of quantum field theoretic anomalies if one includes one right-handed neutrino Weyl fermion field per SM family in the field content, a choice which is otherwise motivated by the fact that it facilitates the see-saw explanation of the light neutrino masses inferred from empirical data. $U(1)_{B_3-L_2}$ is broken near the TeV scale by a *flavon* field, a SM-singlet complex scalar field θ with non-zero $B_3 - L_2$ charge, resulting in a TeV-scale electrically neutral gauge boson, i.e. a Z' state. Much as the Higgs doublet field of the SM possesses a physical state, the Higgs boson, which has been discovered in experiments, so the flavon field contains a physical real scalar state, the flavon particle ϑ.

It is remarkable that a model with spontaneous symmetry breaking at a relatively low (i.e. TeV) scale can pass the experimental bounds upon it coming from flavour constraints. Such constraints are notoriously strict when they involve flavour transitions of the first two generations of electrically charged fermionic fields, particularly from $K - \overline{K}$ mixing [18]. Moreover, the strength of LHC bounds coming from bump hunts in the di-muon mass spectrum resulting from $pp \to Z' \to \mu^+\mu^-$ is diminished by the fact that the Z' only couples with an appreciable strength to *third* family fermions. Thus, the dominant LHC production process (as depicted in the middle panel of figure 1) originates from fusing a bottom quark b and an anti-bottom quark $\bar{b}$ in the initial proton states, providing double suppression to the Z' production cross section from small (anti-)bottom parton distribution functions [19]. Current direct searches imply a lower bound upon the Z' mass $M_{Z'}$ of around 1-2 TeV [2, 3, 20, 21], significantly lower than Z' models in which the Z' field couples to quarks universally, where the current lower bound from ATLAS and CMS is currently around 5 TeV [22, 23]. A window in the parameter space with $20\,\text{GeV} < M_{Z'} < 300\,\text{GeV}$ [2, 3] is all but ruled out at the 95% confidence level [20]. A recent analysis [21] found that although through much of the parameter space the Z' can be discovered at the HL-LHC, either a 3 TeV $\mu^+\mu^-$ collider, a 10 TeV $\mu^+\mu^-$ collider [24] or a 100 TeV FCC-hh collider [25] would cover all of the parameter space compatible with the model's explanation of the $b \to s\mu^+\mu^-$ anomalies.

It is remarkable that a TeV-scale Z', which generates flavour changing neutral currents at the tree-level of perturbation theory, is not only allowed by current data but in fact is motivated by it. Whether or not the $b \to s\mu^+\mu^-$ anomalies persist in collider data, the $B_3 - L_2$ model is of interest both for this reason and because it may be pertinent to

JHEP03(2023)253

the fermion mass puzzle (namely why certain hierarchies within the spectrum of fermion masses and mixings exist). Aside from the aforementioned Z' production, scant collider phenomenology of the model has been studied in terms of direct searches.

It is our purpose here to study the direct collider phenomenology of the flavon in the $B_3 - L_2$ model for the first time. The flavon is expected to have a mass of order $M_{Z'}$ (i.e. the TeV scale) and so may be amenable to direct production and discovery at high energy colliders. We shall see that the flavon field generically mixes with the Higgs field and is therefore bounded by some electroweak measurements and Higgs searches. In detail, we wish to make a first estimate of the current and potential future collider capabilities of observing the flavon via flavonstrahlung [3],[2] a process whose dominant Feynman diagram is depicted in the right-hand panel of figure 1. Observation of a flavon would be an important confirmation of the means of $U(1)_{B_3-L_2}$ gauge symmetry breakdown, since $U(1)_{B_3-L_2}$ breaking could instead be a consequence of the Stueckelberg mechanism [28], which possesses no explicit flavon field. This then has implications for the fermion mass puzzle since, for example, the Froggatt-Nielsen mechanism [29], which can explain the hierarchies between the different families observed in the measured values of the SM fermion masses, necessarily involves a flavon field.

The paper proceeds in section 2 by briefly reiterating some salient points in the construction of the $B_3 - L_2$ model. The Higgs phenomenology of the flavon particle is reviewed in section 3 and current collider constraints upon the parameter space of the $B_3 - L_2$ model are imposed. Then, in section 4, we study the flavonstrahlung process in allowed parts of the parameter space. We shall see that the cross-section is too small to result in a realistic measurement at the HL-LHC (except for a small portion of parameter space in the case that the flavon charge is larger than unity) but that a 10 TeV muon collider of a 100 TeV hadron collider such as the FCC-hh could facilitate discovery of flavonstrahlung and therefore facilitate discovery of the flavon field associated with breaking the gauged flavour symmetry. We summarise and conclude in section 5.

2 $B_3 - L_2$ model

We shall now review some salient points of the construction of the $B_3 - L_2$ model. For definiteness, we use the simple bottom-up construction of ref. [3]. The $B_3 - L_2$ model is constructed by extending the SM gauge group, $SU(3) \times SU(2)_L \times U(1)_Y$, by an abelian factor $U(1)_{B_3-L_2}$ in a direct product. This new symmetry is gauged, so it comes with an electrically neutral force carrier, the Z' boson. We also introduce the flavon field (θ), a SM-singlet complex scalar, which carries charge q_θ under $U(1)_{B_3-L_2}$. Table 1 displays the charges of the fields in the model under the new abelian symmetry. Three right-handed neutrinos $\nu_{R_{1,2,3}}$ are added in order to facilitate neutrino masses and mixing. With these fields and charges, $U(1)_{B_3-L_2}$ acts vectorially on the fermions (i.e. acts in the same way on left-handed chiral fermions as it does on their right-handed partners), and gauge anomaly cancellation manifestly takes place. There is an implicit assumption in the $B_3 - L_2$ model (and other similar models) that they originate from some more complete ultra-violet model

[2] LHC HZ' production has been studied in a family universal $U(1)$ model in refs. [26, 27].

JHEP03(2023)253

Q'_{iL}	u'_{iR}	d'_{iR}	L'_1	L'_2	L'_3	e'_{1R}	e'_{2R}	e'_{3R}
0	0	0	0	-3	0	0	-3	0
ν'_{1R}	ν'_{2R}	ν'_{3R}	Q'_{3L}	u'_{3R}	d'_{3R}	H	θ	
0	-3	0	1	1	1	0	q_θ	

Table 1. The $U(1)_{B_3-L_2}$ charge assignments. A prime stands for a weak eigenstate Weyl fermion and the family index i takes values 1 and 2. The flavon charge q_θ is a non-zero rational number.

which may be a semi-simple extension, thus obviating constraints coming from Landau poles [30].

The fermionic couplings of the Z' are expressed in the Lagrangian density

$$\mathcal{L}_{Z'\psi} = -g_{Z'}\Big(\overline{Q'_{3L}}\not{Z}'Q'_{3L} + \overline{u'_{3R}}\not{Z}'u'_{3R} + \overline{d'_{3R}}\not{Z}'d'_{3R} - 3\overline{L'_{2L}}\not{Z}'L'_{2L} - 3\overline{e'_{2R}}\not{Z}'e'_{2R} - 3\overline{\nu'_{2R}}\not{Z}'\nu'_{2R}\Big) \tag{2.1}$$

where $g_{Z'}$ is the gauge coupling of the new $U(1)_{B_3-L_2}$ symmetry. In order to study the phenomenology of the model, however, we must transform to the mass basis. We denote the 3-component column vectors in family space by boldface letters, $\mathbf{Q_L}' = (\mathbf{u_L}', \mathbf{d_L}')$, $\mathbf{L_L}' = (\mathbf{\nu_L}', \mathbf{e_L}')$, $\mathbf{u_R}'$, $\mathbf{d_R}'$, $\mathbf{e_R}'$ and $\boldsymbol{\nu}'_\mathbf{R}$. The transformation between the (primed) weak eigenbasis and the (unprimed) mass eigenbasis written

$$\mathbf{P}' = V_I\mathbf{P} \tag{2.2}$$

for $I \in \{u_L, d_L, e_L, \nu_L, u_R, d_R, e_R, \nu_R\}$. Encoding the family-dependent couplings of eq. (2.1) into two 3 by 3 diagonal matrices

$$\Xi := \begin{pmatrix} 0 & 0 & 0 \\ 0 & 0 & 0 \\ 0 & 0 & 1 \end{pmatrix}, \quad \Omega := \begin{pmatrix} 0 & 0 & 0 \\ 0 & 1 & 0 \\ 0 & 0 & 0 \end{pmatrix} \tag{2.3}$$

and defining $\Lambda := V_I^\dagger \alpha V_I$ where $I \in \{u_L, d_L, e_L, \nu_L, u_R, d_R, e_R, \nu_R\}, \alpha \in \{\Xi, \Omega\}$, we obtain $\mathcal{L}_{Z'\psi}$ in the mass eigenbasis:

$$\begin{aligned}\mathcal{L}_{Z'\psi} = -g_{Z'}\Big(&\overline{\mathbf{u_L}}\Lambda_\Xi^{(u_L)}\not{Z}'\mathbf{u_L} + \overline{\mathbf{d_L}}\Lambda_\Xi^{(d_L)}\not{Z}'\mathbf{d_L} + \overline{\mathbf{u_R}}\Lambda_\Xi^{(u_R)}\not{Z}'\mathbf{u_R} + \overline{\mathbf{d_R}}\Lambda_\Xi^{(d_R)}\not{Z}\mathbf{d_R} \\ &- 3\overline{\boldsymbol{\nu}_\mathbf{L}}\Lambda_\Omega^{(\nu_L)}\not{Z}'\boldsymbol{\nu}_\mathbf{L} - 3\overline{\mathbf{e_L}}\Lambda_\Omega^{(e_L)}\not{Z}'\mathbf{e_L} - 3\overline{\boldsymbol{\nu}_\mathbf{R}}\Lambda_\Omega^{(\nu_R)}\not{Z}'\boldsymbol{\nu}_\mathbf{R} - 3\overline{\mathbf{e_R}}\Lambda_\Omega^{(e_R)}\not{Z}'\mathbf{e_R}\Big).\end{aligned} \tag{2.4}$$

Provided that $(V_{d_L})_{23} \neq 0$, eq. (2.4) couples the Z' to both $(\bar{b}s + \bar{s}b)$ and $\mu^+\mu^-$. The Z' boson can thus mediate $b \to s\mu^+\mu^-$transitions, thereby influencing B-observables.

The kinetic term of the flavon field reads

$$\mathcal{L}_{\theta,\text{kin}} = (D^\mu\theta)^*(D_\mu\theta), \tag{2.5}$$

with its covariant derivative being

$$D_\mu\theta = \Big(\partial_\mu - ig_{Z'}q_\theta Z'_\mu\Big)\theta. \tag{2.6}$$

JHEP03(2023)253

The flavon field spontaneously breaks $U(1)_{B_3-L_2}$ by developing a non-zero vacuum expectation value (VEV) $\langle\theta\rangle = v_\theta \neq 0$. As a consequence, the Z' acquires a mass $M_{Z'} = q_\theta g_{Z'} v_\theta$. In the unitary gauge, the Z' boson eats the massless Goldstone boson associated with the broken symmetry and obtains a longitudinal polarisation mode. We are left with three Z' degrees of freedom and a single real flavon field, ϑ.

2.1 Spontaneous symmetry breaking

The introduction of a new SM-singlet scalar field, real or complex, modifies the scalar potential of the theory. In addition to the mass and quartic self-interaction terms for the new scalar, the theory also allows for a renormalisable dimension-4 term connecting the Higgs doublet to the beyond the SM (BSM) scalar. Thus, the combined scalar potential for the SM-Higgs doublet (H) and the flavon field (ϑ) in the $B_3 - L_2$ model reads

$$V(H,\theta) = -\mu_H^2 H^\dagger H + \lambda_H (H^\dagger H)^2 - \mu_\theta^2 \theta^* \theta + \lambda_\theta (\theta^* \theta)^2 + \lambda_{\theta H} \theta^* \theta H^\dagger H. \tag{2.7}$$

Scalar potentials of this form have received considerable attention in the past (see for instance [31–33]), and we review here some standard steps. To find the lowest energy state of the potential, we work in the unitary gauge and expand both fields about their vacuum expectation values (VEVs), denoted by v_H and v_θ:

$$H = \begin{pmatrix} 0 \\ \frac{v_H + h'}{\sqrt{2}} \end{pmatrix}, \qquad \theta = \frac{v_\theta + \vartheta'}{\sqrt{2}}. \tag{2.8}$$

Minimising the scalar potential with respect to the VEVs,

$$\frac{\partial V}{\partial v_H} = 0, \quad \frac{\partial V}{\partial v_\theta} = 0, \tag{2.9}$$

gives us the following two expressions:

$$v_H = \sqrt{\frac{4\mu_H^2 \lambda_\theta - 2\mu_\theta^2 \lambda_{\theta H}}{4\lambda_H \lambda_\theta - \lambda_{\theta H}^2}}, \tag{2.10}$$

$$v_\theta = \sqrt{\frac{4\mu_\theta^2 \lambda_H - 2\mu_H^2 \lambda_{\theta H}}{4\lambda_H \lambda_\theta - \lambda_{\theta H}^2}}. \tag{2.11}$$

The requirements that the extremum be a local minimum and the potential bounded from below for large field values provide the constraints

$$4\lambda_H \lambda_\theta - \lambda_{\theta H}^2 > 0, \tag{2.12}$$

$$\lambda_H, \lambda_\theta > 0, \tag{2.13}$$

respectively [32].

When we substitute the VEVs and the expanded scalar fields into eq. (2.7), terms bilinear in h' and ϑ' appear. Writing the quadratic part of the potential as

$$\mathcal{L}_{\text{quadratic}} = -\frac{1}{2} \begin{pmatrix} h' & \vartheta' \end{pmatrix} M^2 \begin{pmatrix} h' \\ \vartheta' \end{pmatrix} \tag{2.14}$$

JHEP03(2023)253

leads to the non-diagonal, symmetric mass matrix

$$M^2 = \begin{pmatrix} \frac{1}{2}\lambda_{\theta H} v_\theta^2 + 3\lambda_H v_H^2 - \mu_H^2 & \lambda_{\theta H} v_H v_\theta \\ \lambda_{\theta H} v_H v_\theta & \frac{1}{2}\lambda_{\theta H} v_H^2 + 3\lambda_\theta v_\theta^2 - \mu_\theta^2 \end{pmatrix},$$
$$= \begin{pmatrix} 2\lambda_H v_H^2 & \lambda_{\theta H} v_H v_\theta \\ \lambda_{\theta H} v_H v_\theta & 2\lambda_\theta v_\theta^2 \end{pmatrix}. \tag{2.15}$$

The matrix M^2 is diagonalised by an orthogonal rotation P, parameterised by an angle ϕ:

$$M^2 = P^T \operatorname{diag}\left(m_h^2, m_\vartheta^2\right) P, \tag{2.16}$$

$$\begin{pmatrix} 2\lambda_H v_H^2 & \lambda_{\theta H} v_H v_\theta \\ \lambda_{\theta H} v_H v_\theta & 2\lambda_\theta v_\theta^2 \end{pmatrix} = \begin{pmatrix} \cos\phi & \sin\phi \\ -\sin\phi & \cos\phi \end{pmatrix} \begin{pmatrix} m_h^2 & 0 \\ 0 & m_\vartheta^2 \end{pmatrix} \begin{pmatrix} \cos\phi & -\sin\phi \\ \sin\phi & \cos\phi \end{pmatrix}. \tag{2.17}$$

Solving for ϕ, we find

$$\sin 2\phi = \frac{2\lambda_{\theta H} v_H v_\theta}{m_\vartheta^2 - m_h^2} \tag{2.18}$$

or, via a double angle formula,

$$\sin\phi = \sqrt{\frac{1}{2}\left(1 - \sqrt{1 - \frac{4\lambda_{\theta H}^2 v_H^2 v_\theta^2}{\left(m_h^2 - m_\vartheta^2\right)^2}}\right)}. \tag{2.19}$$

We have thus obtained the field rotation P, which transforms the primed scalar field basis (h', ϑ') into the (unprimed) mass eigenbasis:

$$\begin{pmatrix} h \\ \vartheta \end{pmatrix} = \begin{pmatrix} \cos\phi & -\sin\phi \\ \sin\phi & \cos\phi \end{pmatrix} \begin{pmatrix} h' \\ \vartheta' \end{pmatrix}. \tag{2.20}$$

The smallest eigenvalue of M^2, m_h^2, and the associated eigenstate h are taken to correspond to the 125 GeV Higgs boson discovered at the LHC experiments, whereas the larger-mass eigenstate ϑ is the flavon boson whose mass is written as m_ϑ.

Expanding the scalar fields about their VEVs and rotating into the mass eigenbasis as described above, the kinetic term $\mathcal{L}_{\theta,\text{kin}}$ yields an interaction term

$$\mathcal{L}_{\theta,\text{kin}} \supset \cos\phi\, g_{Z'}^2 q_\theta^2 v_\theta \vartheta Z'_\mu Z'^\mu. \tag{2.21}$$

This term helps give rise to the flavonstrahlung process depicted in the right-hand panel of figure 1 and it will therefore play a key role in the present study.

The Higgs-flavon axis of the model can be expressed in terms of three parameters: m_ϑ, ϕ and v_θ, the last of which can be decomposed as $v_\theta = M_{Z'}/(q_\theta g_{Z'})$. Accordingly, the quartic couplings λ_H and λ_θ, together with eq. (2.18), become

$$\lambda_H = \frac{m_h^2 \cos^2\phi + m_\vartheta^2 \sin^2\phi}{2v_H^2}, \tag{2.22}$$

$$\lambda_\theta = \frac{m_\vartheta^2 \cos^2\phi + m_h^2 \sin^2\phi}{2v_\theta^2}, \tag{2.23}$$

$$\lambda_{\theta H} = \frac{\sin(2\phi)\left(m_\vartheta^2 - m_h^2\right)}{2v_H v_\theta}. \tag{2.24}$$

JHEP03(2023)253

2.2 Assumptions

We must specify the model further before we can study its phenomenology. In particular, the V_I mixing matrices deserve our attention. With simplicity, ease of passing flavour bounds and the ability to explain the neutral current $b \to s\mu^+\mu^-$ anomalies as guiding principles, an example set of mixing matrices V_I was proposed in ref. [3]:

$$V_{d_L} = \begin{pmatrix} 1 & 0 & 0 \\ 0 & \cos\theta_{sb} & -\sin\theta_{sb} \\ 0 & \sin\theta_{sb} & \cos\theta_{sb} \end{pmatrix}, \tag{2.25}$$

$V_{d_R} = 1, V_{e_R} = 1, V_{e_L} = 1$ and $V_{u_R} = 1$, where here 1 denotes the 3 by 3 identity matrix. These imply that $V_{u_L} = V_{d_L} V^\dagger$ and $V_{\nu_L} = U^\dagger$, where V and U are the CKM and PMNS matrices, respectively. Here, we will adhere to the same set of mixing matrices while keeping in mind that this choice is just intended to provide an example case for further study. This set of fermion mixing matrices results in a Lagrangian containing the terms

$$\mathcal{L} \supset -g_{Z'}\left[\left(\frac{1}{2}\sin 2\theta_{sb}\bar{s}\not{Z}' P_L b + \text{H.c.}\right) - 3\overline{\mu}\not{Z}'\mu\right], \tag{2.26}$$

where P_L is a left-handed spinor helicity projection operator. Once the Z' is integrated out, these terms yield a contribution to the Wilson coefficient $\mathcal{C}_9$ from

$$\mathcal{H}_{\text{WET}} = \ldots + \left[\mathcal{C}_9 \mathcal{N}(\bar{b}\gamma_\alpha P_L s)(\bar{\mu}\gamma^\alpha \mu) + \text{H.c.}\right], \tag{2.27}$$

in the weak effective theory Hamiltonian, which can significantly ameliorate the $b \to s\mu^+\mu^-$ anomalies [4–11]. In eq. (2.27), $\alpha \in \{0, 1, 2, 3\}$ is a space-time index and

$$\mathcal{N} = \frac{4G_F}{\sqrt{2}} V_{tb} V_{ts}^* \frac{\alpha}{4\pi} = 1/(36\ \text{TeV})^2 \tag{2.28}$$

is a normalising constant.

We shall set the flavon charge q_θ equal to 1 unless stated otherwise. The flavonstrahlung cross section is proportional to q_θ^2, so it is straightforward to extend most of our results to different values of the charge.

3 Flavon Phenomenology

In this section we first review the phenomenological constraints on the $U(1)_{B_3-L_2}$ model obtained in earlier work. These limits apply to the parameter set $\{g_{Z'}, M_{Z'}, \theta_{23}\}$, the three inputs which influence the ability of the model to explain $b \to s\mu^+\mu^-$ anomalies. We then move on to study the flavon sector of the theory, obtaining an upper bound on the Higgs-flavon mixing angle ϕ and discussing the leading flavon decay channels.

We have updated the FeynRules [34] implementation of the $U(1)_{B_3-L_2}$ model from ref. [3] by adding the flavon sector, which was previously neglected.[3] We have also used FeynRules to convert the model into UFO format [35].

[3]The model file can be found in the ancillary information of the arXiv version of this work.

JHEP03(2023)253

3.1 Fit to neutral current $b \to s\mu^+\mu^-$ anomalies and LHC constraints

One may use eq. (2.26) to match the $U(1)_{B_3-L_2}$ model to fits of $b \to s\mu^+\mu^-$data, as was done in ref. [3]. This condition lets us eliminate the mixing angle θ_{sb} and leaves us with two free parameters relevant to B decay data: $M_{Z'}$ and $g_{Z'}$. Defining the dimensionless quantity x as

$$x \coloneqq g_{Z'} \frac{1\ \text{TeV}}{M_{Z'}}, \tag{3.1}$$

one obtains

$$\theta_{sb} = \frac{1}{2} \sin^{-1}\left(\frac{-5.1 \times 10^{-4} \mathcal{C}_9}{x^2} \right). \tag{3.2}$$

In this work, we use $\mathcal{C}_9 = -0.73 \pm 0.15$, which is the best-fit value obtained in [36] prior to the recent LHCb updates [16, 17] of the lepton flavour universality ratios R_K and R_{K^*}.

It was found in ref. [3] that there are both lower and upper bounds on the value of x. The lower bound stems from measurements of $B_s - \overline{B_s}$ mixing, which the Z' contributes to at tree-level. The upper bound originates from measurements of the neutrino trident cross-section, $\sigma(\nu_\mu N \to \nu_\mu N \mu^+\mu^-)$, which also receives Z' contributions at tree-level. We are left with the constraint $0.04 < x < 0.67$ [21] which we will adhere to in this work. Substituting such values of x into eq. (3.2) implies that θ_{sb} is small. For small θ_{sb}, the collider phenomenology that we shall discuss is not sensitive to its precise value and so should also be valid for up-to-date fits of $\mathcal{C}_9$ incorporating the recent LHCb results.[4] This is because flavonstrahlung production proceeds initially via Z' production, which dominantly proceeds via $b\bar{b}$ fusion and is proportional to $g_{Z'}^2 \cos^4\theta_{sb} \approx g_{Z'}^2[1 - 2\theta_{sb}^2 + \mathcal{O}(\theta_{sb}^4)]$.

In ref. [20], a set of LHC constraints was recast on the $M_{Z'} - g_{Z'}$ plane of the theory. Figure 10 of that paper shows that the previously allowed light Z' region of parameter space, with $M_{Z'} < 0.3\,\text{TeV}$, is all but ruled out, and in the rest of the paper, we shall assume that $M_{Z'} > 1\,\text{TeV}$. A recent recasting of the CMS high-mass di-lepton searches [23] eliminated at 95% CL all parameter points with $M_{Z'} \lesssim 2$ TeV [21].

3.2 Perturbativity of Z' couplings

Neglecting fermion massess in comparison with $M_{Z'}$, the partial decay rate of the Z' turning into a pair of Weyl fermions reads

$$\Gamma\left(Z' \to f_i \bar{f}_i\right) = \frac{C_i}{24\pi} (q_i g_{Z'})^2 M_{Z'}, \tag{3.3}$$

where C_i is the number of colour degrees of freedoms of the fermion f_i, and q_i is its $U(1)_{B_3-L_2}$ charge[5] in units of $g_{Z'}$, as assigned in table 1. Summing over all fermion species (except for the right-handed neutrinos which are assumed to be more massive than the Z') yields the equation

$$\frac{\Gamma}{M_{Z'}} = \frac{13 g_{Z'}^2}{8\pi} \tag{3.4}$$

[4] See [37] for a recent fit.

[5] Note that $\Gamma/M_{Z'}$ is independent of rescaling all charges by absorbing the scaling in $g_{Z'}$.

JHEP03(2023)253

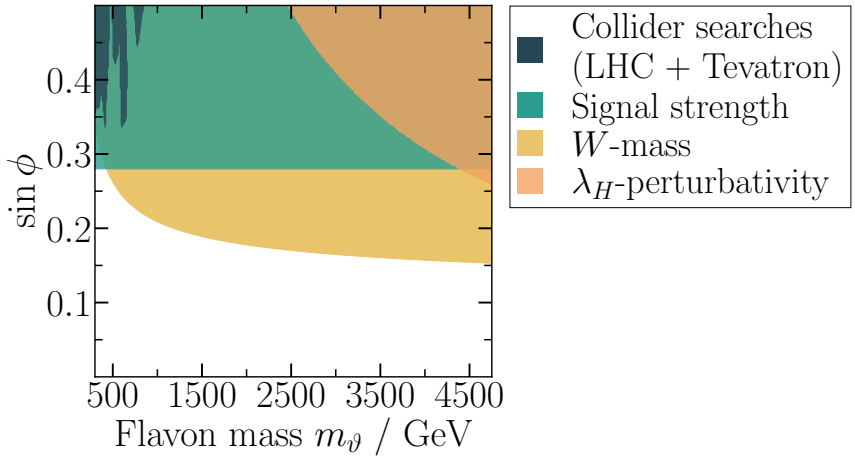

Figure 2. 95% CL limits on the Higgs-flavon mixing angle stemming from direct Higgs searches at the LHC and Tevatron (obtained using HiggsBounds), ATLAS signal strength measurements, the W boson mass and perturbativity of λ_H. The white region is currently allowed. To obtain the M_W-bound, we have assumed $g_{Z'} = 0.15, M_{Z'} = 3\,\text{TeV}$, but because M_W is only very weakly dependent on the Z' parameters, we will use this bound for all values of $M_{Z'}$ and $g_{Z'}$ considered in this work.

where Γ is the total width of the Z'. We impose the limit $\Gamma/M_{Z'} < 1/3$ to ensure that our perturbative cross-section calculations remain valid. This translates into $g_{Z'} < \sqrt{8\pi/39} = 0.80$. The perturbativity condition together with a fit to $b \to s\mu^+\mu^-$ data lead to an upper bound on the Z' mass: $M_{Z'} < 20\,\text{TeV}$.

3.3 Constraints on the mixing angle ϕ

There are numerous experimental and theoretical constraints on the Higgs-flavon mixing angle ϕ. These are discussed at length in, e.g. refs. [33, 38, 39] in the context of the real singlet extension of the SM. We expect the constraints to be largely the same in the $B_3 - L_2$ model, as most constraints are independent of the presence of the Z' and the extra degree of freedom from the complexity of the flavon field. Because the $B_3 - L_2$ model is seen as a low energy effective theory, we disregard some theoretical constraints, namely perturbative unitarity of scattering amplitudes in the high energy limit and the lack of Landau poles below the Planck scale [30]. In this work, we impose four constraints on the $B_3 - L_2$ model: limits from direct Higgs searches at hadron colliders, the Higgs signal strength measurements, agreement with the experimentally measured W boson mass and perturbativity of the Higgs-quartic couplings at the scale of the effective theory. These correspond to the four coloured regions in figure 2.

3.3.1 Higgs signal strength

The rotation into the mass eigenbasis of the scalar fields in eq. (2.20) modifies all SM Higgs couplings by a factor of $\cos\phi$. The Higgs signal strength, defined as the production cross-section times branching ratio (BR) normalised to the SM prediction, $\mu := (\sigma \times \text{BR})_{\text{obs}}/(\sigma \times \text{BR})_{\text{SM}}$ for a given Higgs production and decay mode, is then predicted to be $\mu = \cos^2\phi$

JHEP03(2023)253

irrespective of the mode. The ATLAS and CMS Run 2 combination results for the global signal strength read $\mu_{\text{ATLAS}} > 0.92$, $\mu_{\text{CMS}} > 0.90$ at 95 % CL [40]. The more stringent of the two, μ_{ATLAS}, yields for the Higgs-flavon mixing angle: $|\sin\phi| < 0.28$. This limit on $\sin\phi$ is independent of the flavon mass.

3.3.2 Direct searches

We utilise the public code HiggsBounds 5.3.2beta [41–46] to obtain 95% CL direct search limits on an extra scalar field from the LHC and Tevatron. This bound is stronger at lower flavon masses and starts to wane for $m_\vartheta \gtrsim 750\,\text{GeV}$; the constraint is visible on the upper left-hand side of figure 2.

3.3.3 Perturbativity of quartic couplings

For the theory to remain perturbative, we will enforce the conditions $|\lambda_H, \lambda_\theta, \lambda_{\theta H}| < 4\pi$ on the quartic couplings. For most values of the ratio $x = g_{Z'}\,\text{TeV}/M_{Z'}$ in its allowed region $x \in [0.04, 0.67]$ the quartic Higgs coupling λ_H, which is independent of x, places a more stringent bound on $\sin\phi$ than either $\lambda_{\theta H} \propto x$ or $\lambda_\theta \propto x^2$. The constraint arising from perturbativity of λ_H corresponds to the orange region in figure 2. At the end of the allowed interval, where $x \sim 0.6$, the bound from λ_H is superseded by $\lambda_{\theta H}$. However, for $m_\vartheta \lesssim 5\,\text{TeV}$, neither of these limits is competitive against the bound coming from M_W measurements. For flavon masses much more massive than this, the perturbativity of the couplings becomes the tightest constraint on the mixing angle. This can be phrased in another way: for a given mixing angle, there is an upper bound on the flavon mass coming from perturbativity of the three quartic couplings. The strictest bound may depend on x and the flavon charge q_θ, but λ_H will always provide an upper limit independent of x and q_θ.

3.3.4 *W* boson mass

We now investigate the prediction of the W boson mass in the $B_3 - L_2$ model. In the real singlet extension of the SM, for an extra scalar field more massive than $\sim 300\,\text{GeV}$, agreement between the experimentally measured W boson mass M_W and the model prediction at the one-loop level places a bound more austere than that arising from the oblique S, T and U parameters [47]. The Z' boson cannot influence the oblique parameters in the $B_3 - L_2$ model, but it does affect M_W via Z'-induced vertex corrections, as we will see. We thus posit that M_W will provide the stricter of the two limits in the $B_3 - L_2$ model, too, and confirm the assertion by calculating the W boson mass in the model.

Predicting the value of M_W is based on matching the 4-Fermi theory muon lifetime with the 1-loop calculation using the full Lagrangian of the theory (see [48–51] for more detailed accounts). The matching yields an expression connecting the experimentally measured Fermi coupling constant G_F to the parameters of the $B_3 - L_2$ model:

$$\frac{G_F}{\sqrt{2}} = \frac{e^2}{8 M_W^2 \sin^2\theta_W}(1 + \Delta r), \tag{3.5}$$

JHEP03(2023)253

where Δr contains all of the loop corrections to the decay process in the full theory. Taking M_Z, G_F and α as experimental inputs and working with the on-shell definition of the weak mixing angle where $\sin^2\theta_W = 1 - M_W^2/M_Z^2$ to all orders in perturbation theory, we can rearrange the above equation to obtain a prediction for the W-boson mass:

$$M_W^2 = \frac{1}{2}M_Z^2\left[1 + \sqrt{1 - \frac{4\pi\alpha}{\sqrt{2}G_F M_Z^2}\left[1 + \Delta r(M_W^2)\right]}\right]. \tag{3.6}$$

Given a small perturbation $\delta(\Delta r)$, resulting from BSM physics, the W boson mass changes by

$$\Delta M_W \simeq -\frac{1}{2}M_W \frac{\sin^2\theta_W}{\sin^2\theta_W - \cos^2\theta_W}\delta(\Delta r). \tag{3.7}$$

At the one-loop level in the $U(1)_{B_3-L_2}$ model, there are two kinds of BSM contributions to Δr:[6] those arising from Z'-vertices (figure 3) and those arising from Higgs-flavon mixing (figure 4), which were evaluated in ref. [47] and will always act to make the W boson lighter. Each of the two sets of diagrams depends on different parameters: the size of the Z' vertex contributions is a function of $\{M_{Z'}, g_{Z'}\}$ whereas Higgs-flavon mixing hinges on $\{\sin\phi, m_\vartheta\}$.

We employ the FeynArts, FormCalc and LoopTools packages (versions 3.11, 9.9 and 2.16, respectively) [52, 53] to aid with the calculation and to evaluate the results numerically. Ignoring terms of order m_μ^2/M_W^2 and $m_\mu^2/M_{Z'}^2$, the Lorentz structure of the $U(1)_{B_3-L_2}$ amplitude is identical to that of the 4-Fermi theory and we can match the two theories at the amplitude level. In doing so, we find that $\delta(\Delta r)$ is dominated by the oblique corrections to the vector boson propagators, overwhelming the Z'-induced effects by several orders of magnitude. The reason is that all of the Z'-effects are of order $g_{Z'}^2 m_\mu^2/M_{Z'}^2$ and thus become negligible for a TeV scale Z'. Thus, the resulting constraint on $\sin\phi$ is essentially independent of $M_{Z'}$ and $g_{Z'}$.

We proceed by comparing the theoretical prediction with the experimentally determined W boson mass and insist on agreement at the 2σ level. The empirical and SM-predicted values of M_W are obtained from the Particle Data Group [40]. For the experimentally measured M_W, we use the current world average (prior to the 2022 CDF measurement[7]), $M_W^{\rm exp} = 80.377 \pm 0.012\,\text{GeV}$, whereas the SM prediction stands at $M_W^{\rm th} = 80.356 \pm 0.006\,\text{GeV}$. Combining the two errors in quadrature, we use eq. (3.7) to obtain a $U(1)_{B_3-L_2}$ model prediction for the mass of the W boson and require that the predicted and measured values disagree by less than 2σ. This constraint corresponds to the yellow region in figure 2 and is the most stringent for $0.5 < m_\vartheta/\text{ TeV} < 5$.

3.4 Flavon decay channels

As the flavon couples to SM fields only through mixing with the Higgs field, its tree-level decay channels resemble those of the SM Higgs whenever $\sin\phi \neq 0$. A key difference,

[6] We neglect loops containing $\ell\ell h$- and $\ell\ell\vartheta$-vertices, for $\ell = e, \mu$, as their contributions are of order $m_\ell^2/v_H^2 \ll 1$.

[7] If the 2022 CDF measurement is considered, all non-zero mixing angles are ruled out at the 2σ level. The $U(1)_{B_3-L_2}$ model can only make the W boson lighter than predicted by the SM, thus *increasing* the tension between experiment and theory.

JHEP03(2023)253

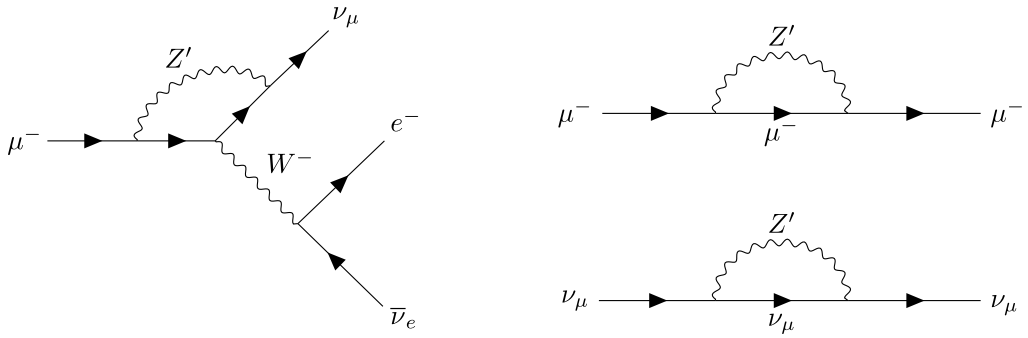

Figure 3. The Z'-induced vertex and self-energy corrections contributing to the Δr parameter. There are no contributions from similar diagrams but with the flavon Goldstone replacing the Z' in the loop because the $U(1)_{B_3-L_2}$ symmetry is vectorial and does not come with a Yukawa sector.

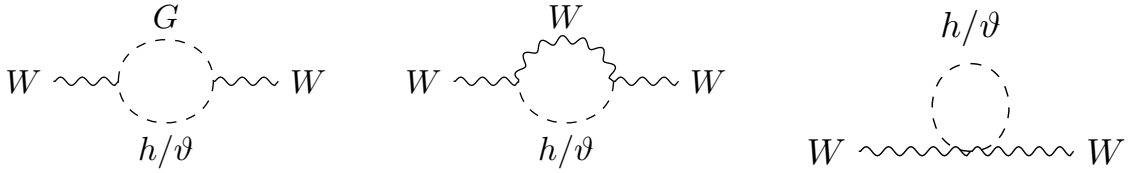

Figure 4. Feynman diagrams corresponding to the three W boson self-energy contributions involving the Higgs boson. We work in the Feynman gauge ($\xi = 1$) and G stands for the charged SM Goldstone boson. Each SM h-vertex is suppressed by a factor of $\cos\phi$ after the Higgs field mixes with the flavon field, but this is complemented by a set of identical diagrams with the physical flavon field running in the loop. Though not drawn here, the Z-boson self-energies are modified in a similar manner.

however, is that the flavon is assumed to be considerably heavier than the Higgs, which allows decays into on-shell W^-W^+, ZZ and $t\bar{t}$ final states. Assuming a TeV scale flavon and Z', and that $m_\vartheta < 2M_{Z'}$ (which covers most of the parameter space studied in this work), there are three channels that dominate the flavon decay rate. The leading channel is $\vartheta \to WW$ with tree-level partial width

$$\Gamma_{\vartheta\to WW} = \frac{m_\vartheta^3 \sin^2\phi}{16\pi v_H^2} + \mathcal{O}\left(\frac{M_W^2}{m_\vartheta^2}\right). \tag{3.8}$$

This is followed by $\vartheta \to hh$ (obtained with FeynRules):

$$\Gamma_{\vartheta\to hh} = \frac{m_\vartheta^3 \cos^4\phi \sin^2\phi}{32\pi v_H^2} + \mathcal{O}\left(\frac{M_W^2}{m_\vartheta^2}\right) + \mathcal{O}\left(\frac{v_H}{v_\theta}\right) \tag{3.9}$$

and $\vartheta \to ZZ$:

$$\Gamma_{\vartheta\to ZZ} = \frac{m_\vartheta^3 \sin^2\phi}{32\pi v_H^2} + \mathcal{O}\left(\frac{M_Z^2}{m_\vartheta^2}\right). \tag{3.10}$$

These expressions lead to the relation $\Gamma_{\vartheta\to WW}/\Gamma_{\vartheta\to hh} \approx 2 \approx \Gamma_{\vartheta\to WW}/\Gamma_{\vartheta\to ZZ}$, which is clearly demonstrated in figure 5. The leading fermionic final state is a $t\bar{t}$ pair because the

JHEP03(2023)253

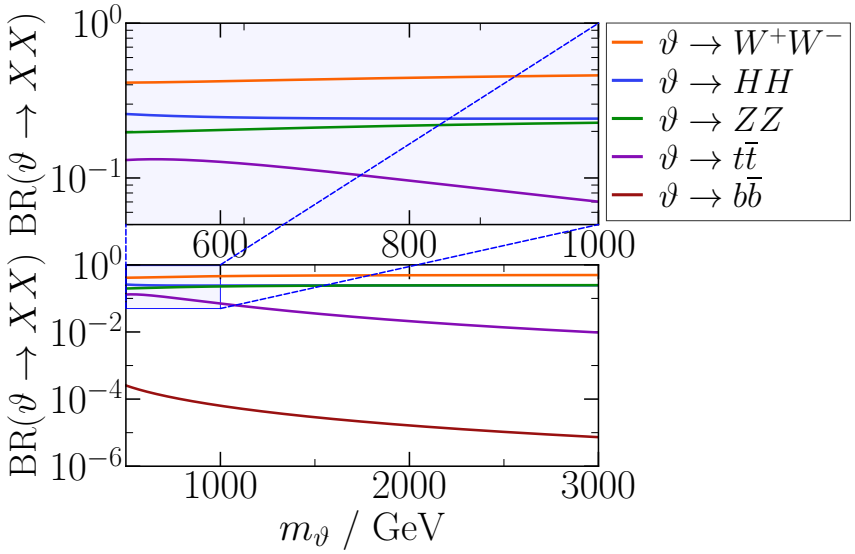

Figure 5. Tree-level flavon BRs for the case $m_\vartheta < 2M_{Z'}$ so that the flavon is unable to decay into a pair of on-shell Z' bosons. The three leading final states, WW, ZZ and hh, come in the approximate ratio 2:1:1. The upper panel is an enlargened version of the shaded region of the lower panel.

top quark Yukawa coupling is the largest Yukawa coupling in the SM. We have evaluated the BRs numerically using MadWidth [54].

We may also study the case with $m_\vartheta > 2M_{Z'}$, although, owing to the constraint $M_{Z'} \gtrsim 2\,\mathrm{TeV}$, this necessarily takes us to multi-TeV flavon masses. If one allows for a flavon mass of order 10 TeV, the decay $\vartheta \to Z'Z'$ can become one of the leading channels. This is shown in figure 6 where the BR into a pair of Z's keeps increasing rapidly as more phase space is made available by lowering $M_{Z'}/m_\vartheta$. To obtain the figure, we have arbitrarily picked $m_\vartheta = 12\,\mathrm{TeV}$, $\sin\phi = 0.05$ and $g_{Z'} = 0.5$. The pink region is excluded at the 95% CL by LHC data, as shown in figure 10 of ref. [21]. This constraint, which is a function of $g_{Z'}/M_{Z'}$, is included for completeness only — the primary purpose of the figure is to show how the mass ratio influences the BRs.

4 Flavonstrahlung at Colliders

We now proceed to study the tree-level flavonstrahlung cross-section at hadron and muon colliders of varying centre-of-mass energies (the dominant Feynman diagram is shown again in figure 7). Flavonstrahlung would likely not be the first detectable direct BSM signal in the $U(1)_{B_3-L_2}$ model, as it is more probable that exclusive Z' production would be observed at lower energies and luminosities. As to whether flavonstrahlung would be the first sign of the flavon particle depends primarily on the value of the Higgs-flavon mixing angle. For sizeable mixing angles, we may discover the flavon through the conventional SM Higgs production processes before reaching the energies and luminosities required for flavonstrahlung. However, observations of Z' and flavon resonances alone would not tell us

JHEP03(2023)253

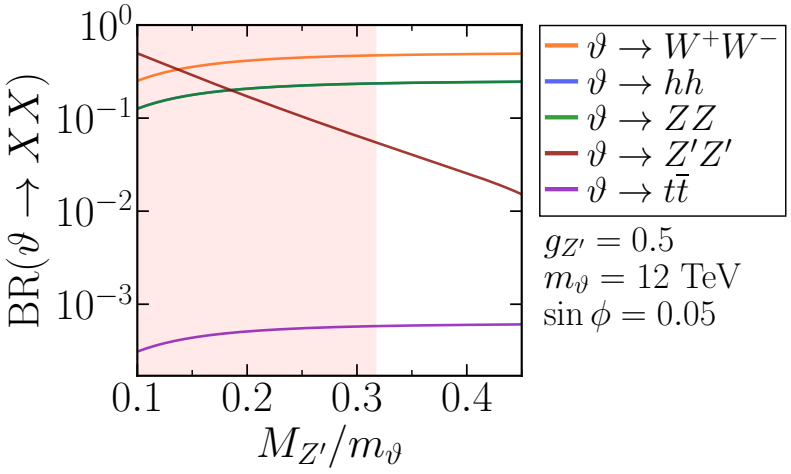

Figure 6. Flavon BRs as a function of the mass ratio $M_{Z'}/m_\vartheta$ when the flavon is much heavier than the Z' and the $U(1)_{B_3-L_2}$ gauge coupling is order one. As the mass ratio is lowered, we see that the $Z'Z'$ final state becomes increasingly important. The region excluded at the 95% CL by LHC data, for this particular choice of parameters, is shown in pink. The green and blue lines are overlap to such a degree that they are indistinguishable by eye.

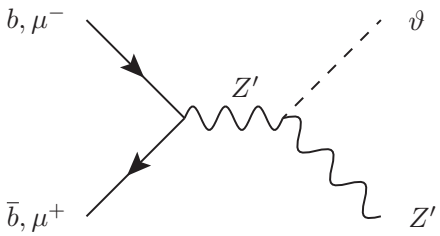

Figure 7. Flavonstrahlung at a hadron collider or a muon collider.

whether the two particles interact with each other and whether the scalar field is involved in generating the Z' mass. Flavonstrahlung is unique in that it combines the Z' and flavon in a single process. The subsequent decays of the Z' and ϑ via their leading channels, $Z' \to \mu^-\mu^+$ and $\vartheta \to W^-W^+$, yield the final state $W^+W^-\mu^+\mu^-$ with a WW resonance at the flavon mass m_ϑ and a di-muon resonance at $M_{Z'}$. As we have seen, the flavon may also decay to ZZ or HH with sizeable BRs, and we leave it for future work to determine which channel is best for flavonstrahlung hunting.

It should be noted that there are two resonant contributions to the flavonstrahlung cross-section: in addition to $pp \to Z'^* \to Z'\vartheta$ (case 1), discussed above, the cross-section also picks up a contribution from $pp \to Z' \to Z'^*\vartheta$ (case 2), where the intermediate Z' is on-shell. Choosing for concreteness the leading decay channels $Z' \to \mu^-\mu^+$ and $\vartheta \to W^-W^+$, case 2 yields a resonance peak in the invariant mass of the 4-particle final state at $q^2 = M_{Z'}^2$ as opposed to the di-muon resonance in case 1. We use the event generator MadGraph5_aMC@NLO v.3.4.1 [55] (abbreviated "MG5_aMC" in the following) to illustrate the two resonances schematically in figure 8 for the final state $\mu^+\mu^-W^+W^-$ at a hadron collider. The orange and red lines corresponds to cases 1 and 2, respectively. We

JHEP03(2023)253

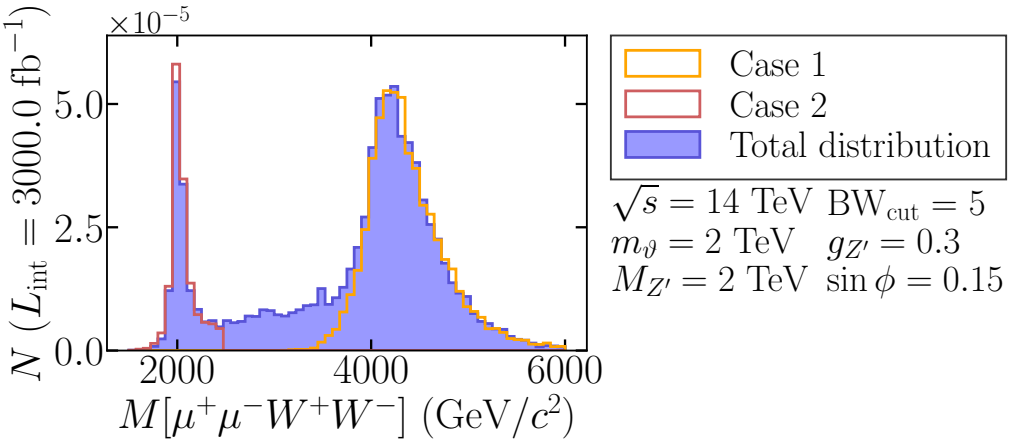

Figure 8. Illustration of the two resonant contributions to the flavonstrahlung cross-section for the leading $\mu^+\mu^- W^+W^-$ final state. The blue region shows the final state invariant mass distribution in the absence of SM backgrounds at the 14 TeV HL-LHC. The orange curve delineates the contribution arising from case 1, where the second Z' in figure 7 is on-shell, whereas the red curve corresponds to case 2, where the first Z' is on-shell.

have used the condition $|M^* - M| < 5\Gamma$ as the definition of a propagator being on-shell, with M^* the invariant mass of the four-momentum carried by the propagator and M and Γ the pole mass and width of the particle. This is achieved using the BW_{cut} parameter in MG5_aMC.

As to which resonance contributes more to the cross-section depends on the partonic energy and the masses of the flavon and Z'. Because case 2 entails lower centre-of-mass energies than case 1, it is more prevalent at lower energy colliders such as the HL-LHC or a 3 TeV muon collider which may lack high enough partonic energies to put both a TeV scale Z' and ϑ on-shell simultaneously. Case 1, on the other hand, is favoured at higher energy colliders such as the FCC-hh or a 10 TeV muon collider where the sum of the Z' and ϑ masses is less than the partonic centre of mass energy for a substantial fraction of collisions.

In order to capture contributions from both resonances in our cross-section computations, we shall study the process $pp \to Z' \to \vartheta Z' \to \vartheta\mu^+\mu^-$, where the rightmost Z' propagator in the Feynman diagram of figure 7 splits into a di-muon pair.[8] We require only that the final state flavon and muons are on-shell, thus allowing both case 1 and case 2 from above to contribute to the total amplitude. Concentrating on the di-muon final state is well-motivated by its clean experimental signature, as well as the large $Z' \to \mu^+\mu^-$ branching ratio, making it the most promising mode for observing flavonstrahlung.

In the presence of non-zero Higgs-flavon mixing, a $Z'\vartheta$ final state may also be produced at tree-level via a t-channel bottom quark or muon exchange. These processes are shown in figure 9. The associated matrix elements are suppressed because the ϑbb- and $\vartheta\mu\mu$-vertices

[8] All flavonstrahlung cross-sections reported hereafter are computed for the $\vartheta\mu^+\mu^-$ final state, even when not explicitly stated.

JHEP03(2023)253

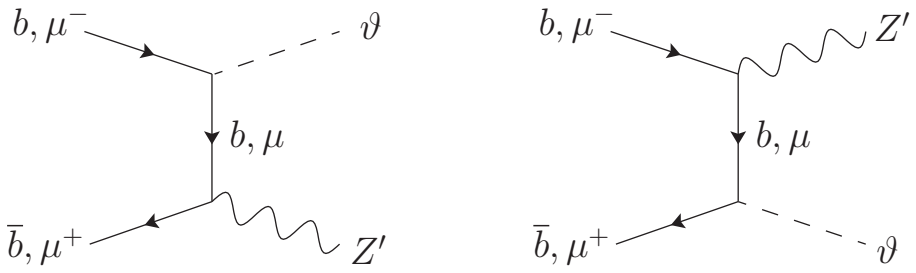

Figure 9. Flavon production with an associated Z' via a t-channel fermion exchange. The bottom quark exchange corresponds to hadron colliders, whereas muon exchange is possible at muon colliders. For the regions of parameter space considered in this work, the contribution to the $\vartheta Z'$ production cross-section from this channel is typically of order 0.1% or less.

come with couplings $\sin\phi(m_b/v_H)$ and $\sin\phi(m_\mu/v_H)$, respectively. Assuming $\sin\phi \sim 0.1$, the inclusion of the t-channel exchange typically changes the $\vartheta Z'$ production cross-sections by approximately 0.1% and never by more than around 3%. We thus neglect contributions arising from the t-channel fermion exchange in this work.

4.1 Flavonstrahlung at Hadron Colliders

We import the UFO model file into MG5_aMC and use it to calculate leading-order flavonstrahlung cross-sections for proton-proton (pp) collisions. The largest partonic contribution to Z' production comes from the $b\bar{b}$ initial state. We thus use the five-flavour parton distribution function (PDF) NNPDF2.3LO where the b quark is absorbed into the proton and jet definitions and treated as massless. There are also negligible contributions to the cross-sections from $s\bar{b}$, $b\bar{s}$ and $s\bar{s}$ initial states, which are nevertheless included in our numerical estimates.

We apply the default MG5_aMC cuts on the phase space of the di-muon pair throughout the computations. Placing cuts according to the specifications of each detector studied in this work would have a negligible impact on our results, and the designs of future detectors are not yet fixed anyway. We thus require that the final-state muon isolation satisfy $\Delta R > 0.4$ and that transverse momenta and pseudo-rapidities of the muons fulfil the conditions $p_T > 10\,\text{GeV}$ and $|\eta| < 2.5$. No cuts are applied on the final state flavon.

To study the process, we select currently allowed combinations of $\{M_{Z'}, g_{Z'}\}$, and compute the flavonstrahlung cross-section as a function of the flavon mass. These combinations are illustrated in the left-hand panel of figure 10 which is adapted from figure 10 of ref. [21]. The region above the solid black line has been excluded at the 95% CL by the CMS high-mass Drell-Yan searches. The dashed blue lines mark the condition $0.04 < x < 0.67$, whereas the green lines delineate perturbativity conditions. We have added five coloured stars representing example parameter combinations to the plot for which we compute benchmark cross-sections. A representative value of the Higgs-flavon mixing angle, $\sin\phi = 0.15$, is chosen in all simulations, keeping in mind that the flavonstrahlung cross-section is proportional to $\cos^2\phi$. We also keep the flavon charge q_θ at unity for now.

JHEP03(2023)253

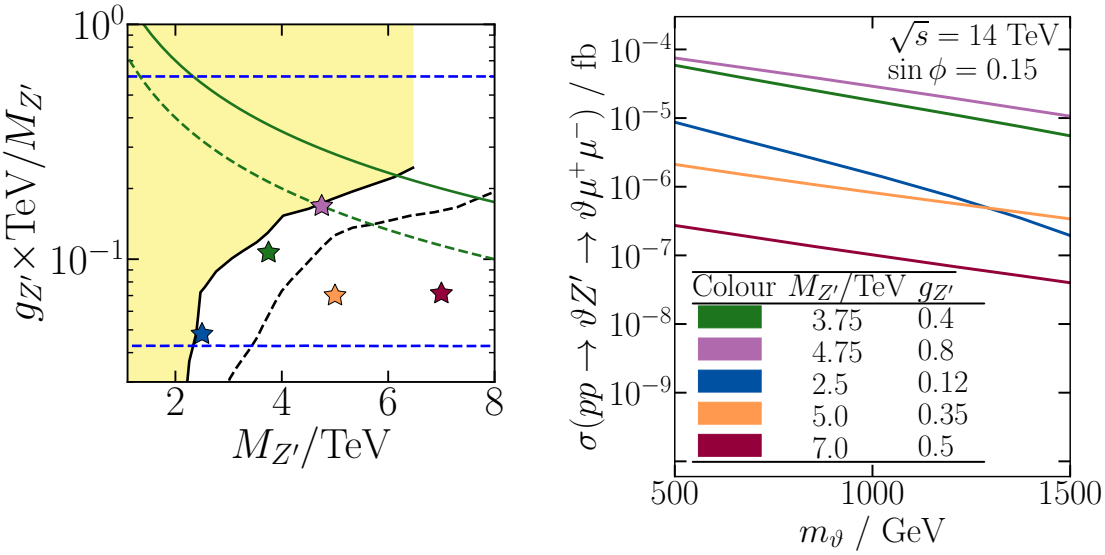

Figure 10. The left-hand panel, based on figure 9 of ref. [21], shows the $g_{Z'} - M_{Z'}$ plane of the parameter space. Everything above the solid black line is excluded at the 95% CL by the LHC whereas the dashed black line indicates the projected 95% CL sensitivity of the HL-LHC. The dashed and solid green lines indicate the $\Gamma/M_{Z'} = 1/3$ and $\Gamma/M_{Z'} = 1$ bounds, above which perturbative computations become inaccurate. The region between the blue dashed lines is the region allowed by the fits discussed in section 3.1. Were another fit including the new R_K and R_{K^*} measurements [16, 17] to be performed, the position of the lower blue line would be revised downward. Coloured stars have been superposed on the figure, with each star labelling a benchmark point in the parameter plane. The right-hand panel shows tree-level flavonstrahlung cross-sections for 14 TeV pp collisions with the flavon charge q_θ set to unity. Each coloured line corresponds to a parameter space point labelled by a star of the same colour.

We first consider the cross-section $\sigma(pp \to \vartheta Z' \to \vartheta\mu^+\mu^-)$ at a centre-of-mass energy $\sqrt{s} = 14\,\mathrm{TeV}$, representing the HL-LHC. The cross-sections for the five example points are shown in the right-hand panel of figure 10, where the colours of the lines correspond to the colours of the stars in the left-hand panel. The exact choices of $\{M_{Z'}, g_{Z'}\}$ are listed in the legend. Assuming HL-LHC integrated luminosity of 3000 fb^{-1}, the plot suggests we expect to produce less than $\mathcal{O}(1)$ flavonstrahlung events. Thus, the flavonstrahlung cross-sections are too small for discovery at the HL-LHC.

Figure 11 shows how the picture changes if the flavon charge q_θ, which can be any rational number, is varied. We have selected the two parameter combinations from figure 10 which yield the largest and third largest cross-sections and let q_θ take values 3, 5 and 10. We find that for flavon charges $q_\theta \gtrsim 5$ and for Z' masses and couplings near the current exclusion limits, the HL-LHC may be able to discover flavonstrahlung up to around 1 TeV flavon masses, but a detailed study would be necessary to confirm this. Either way, the above relies on a finely tuned selection of input parameters and does not change the overall conclusion the HL-LHC lacks sufficient partonic energies and luminosity to look for flavonstrahlung in more than a corner of the currently available parameter space. For the rest of the present paper, we return to flavon charges of unity.

JHEP03(2023)253

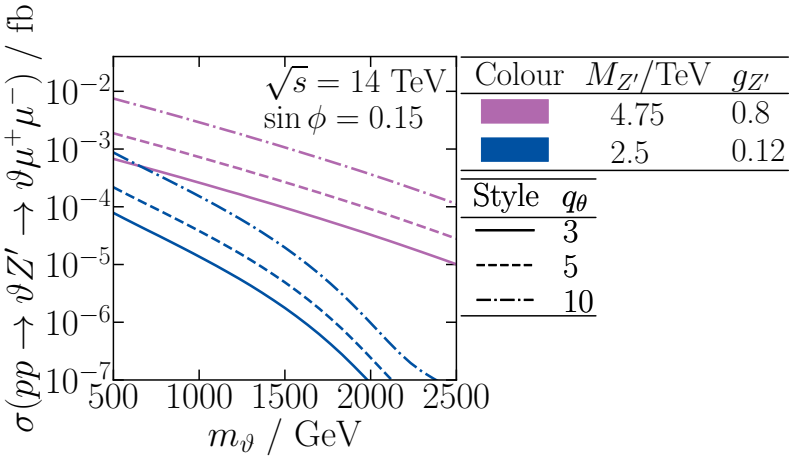

Figure 11. Flavonstrahlung cross-sections for 14 TeV pp collisions but with a variable flavon charge. The charge q_θ takes on values 3, 5 and 10, represented by solid, dashed and dash-dotted lines, respectively. The line colours represent different points in the $M_{Z'}$ — $g_{Z'}$ plane and are congruent with the colours of the stars in figure 10.

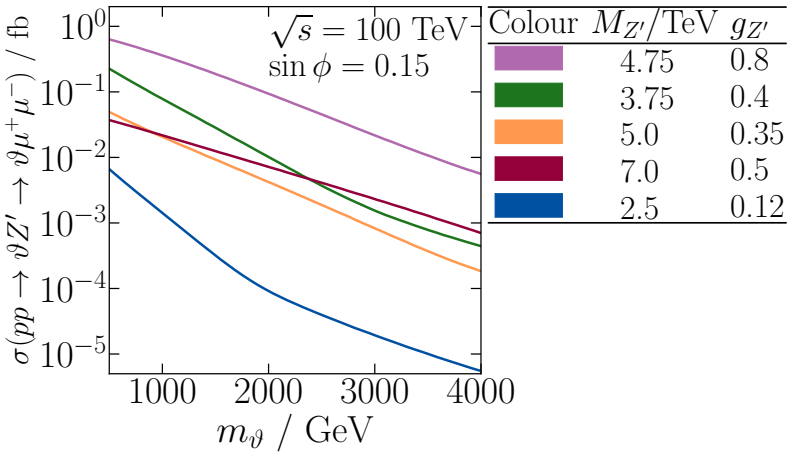

Figure 12. Tree-level flavonstrahlung cross-sections for 100 TeV pp collisions for $q_\theta = 1$. Each coloured line corresponds to a parameter space point labelled by a star of the same colour in figure 10.

We now examine whether a 100 TeV hadron collider, such as the FCC-hh with an integrated luminosity of 20–30 ab^{-1}, would be capable of discovering flavonstrahlung. The simulated cross-sections for the five parameter space points indicated by the coloured stars in figure 10 are shown in figure 12. The resulting cross-sections are greatly enhanced compared to HL-LHC and the larger partonic energies come with the benefit that the cross-sections are not as sensitive to the flavon and Z' masses.

To gain some insight into the reach of the collider, we discard as undiscoverable those parameter space points where less than 10 flavonstrahlung events are expected to be produced. Parameter space points passing this very rough criterion are not automatically within the reach of the collider, and we leave for a future work the detailed study of the

JHEP03(2023)253

SM backgrounds and detector effects which would allow for a more precise estimate of the collider sensitivity. Applying this crude method, we find that for all but the smallest allowed values of the gauge coupling, $g_{Z'} \gtrsim 0.4$, the collider can explore the parameter space up to $\sim 5\,\text{TeV}$ flavon and Z' masses. For $g_{Z'} \lesssim 0.4$, the mass reach will likely be more limited. The blue line in figure 12, corresponding to the smallest allowed coupling for a 2.5 TeV Z' boson, demonstrates that even in this case we may have sensitivity up to a flavon mass of around 2 TeV.

4.2 Flavonstrahlung at Muon Colliders

We may also simulate flavonstrahlung at 3 TeV and 10 TeV $\mu^+\mu^-$ colliders assumed to reach integrated luminosities of 1 ab^{-1} and 10 ab^{-1}, respectively. Despite the centre-of-mass energies being lower than that of the FCC-hh, the fact that nearly all of the beam energy is typically carried by the colliding muon pair may allow these colliders to have high sensitivity to flavonstrahlung. We once again focus on the five example points from figure 10 and use MG5_aMC to perform the simulations. The results for the 3 TeV and 10 TeV colliders are shown in figures 13 and 14, respectively.

The cross-sections do not include initial state radiation (ISR) effects, as this feature is not yet implemented in MG5_aMC. Due to the fact that lepton PDFs peak at momentum fraction $x = 1$, the inclusion of ISR effects is not expected to change the cross-sections dramatically. In a similar fashion to [56], we estimate the magnitude of ISR by allowing for a single collinearly emitted photon in the final state with kinematic parameters such that the photon falls outside the acceptance of the detector. To this end, we enforce that the pseudorapidity η of the photon be in the domain $2.5 < |\eta| < 1000$ and require that its transverse momentum p_T satisfy $0.001\,\text{GeV} < p_T < 0.1\,\text{GeV}$. The inclusive collinear photon is found to increase the cross-sections by $\sim 30\%$ in the case of 10 TeV muon collisions. The cross-sections of figures 13 and 14 do not include the collinearly emitted photon, and one should take them as lower estimates of the real cross-section.

Using the same discoverability criterion as before, we observe in figure 13 that the cross-sections at the 3 TeV collider are large enough to explore regions of the parameter space satisfying $M_{Z'} \lesssim 5\,\text{TeV}$ and $m_\vartheta \lesssim 2.5\,\text{TeV}$ with good sensitivity. Barring very small flavon charges $q_\theta \ll 1$, the 3 TeV collider would likely be able to discover or rule out flavonstrahlung in this region of m_ϑ and $M_{Z'}$. For Z' masses larger than $\sim 5\,\text{TeV}$, the amplitudes are increasingly suppressed by the off-shell Z' propagators, whereas flavon masses of order 3 TeV and greater are unreachable because the collider would be unable to produce an on-shell flavon in the final state.

Similarly, the 10 TeV muon collider has an excellent reach in the parameter space region where $M_{Z'} \lesssim 15\,\text{TeV}$ and $m_\vartheta \lesssim 8\,\text{TeV}$. As figure 14 shows, the flavonstrahlung cross-sections are very sensitive to the size of the coupling $g_{Z'}$ (they scale as[9] $g_{Z'}^4$) compared with sensitivity to m_ϑ and $M_{Z'}$. The cross-sections are greater than around 10^{-1} fb for even the smallest allowed values of the coupling, meaning that the 10 TeV collider would likely be able to cover all of the parameter space , at least when q_θ is of order one or more.

[9] Note that the cross-section scales as $g_{Z'}^6 v_\vartheta^2$, but at a fixed value of $M_{Z'}$, $v_\vartheta \propto 1/g_{Z'}$.

JHEP03(2023)253

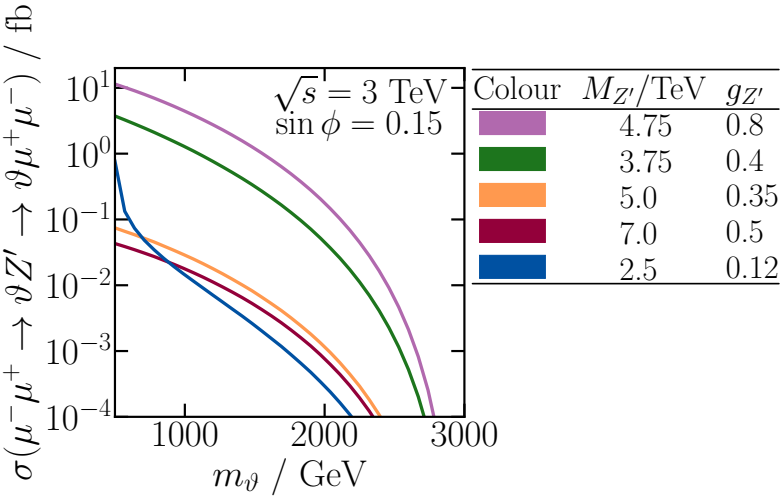

Figure 13. Tree-level flavonstrahlung cross-sections for 3 TeV $\mu^+\mu^-$ collisions for $q_\theta = 1$. Each coloured line corresponds to a parameter point labelled by a star of the same colour in figure 10. The cross-sections do not include ISR effects.

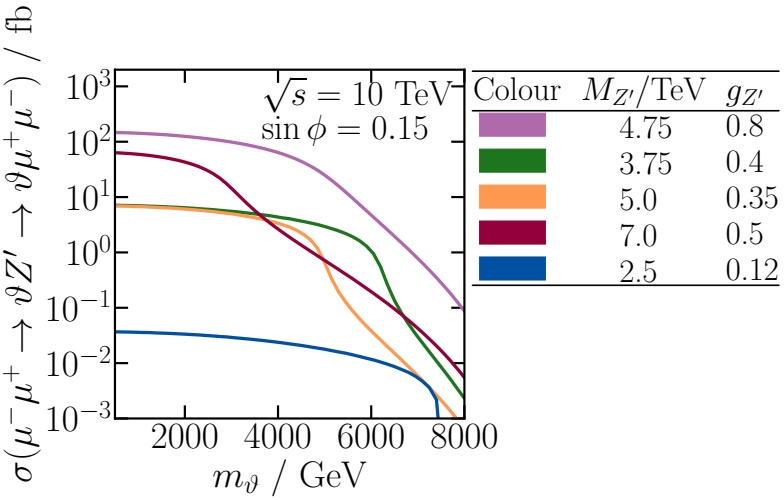

Figure 14. Tree-level flavonstrahlung cross-sections for 10 TeV $\mu^+\mu^-$ collisions for $q_\theta = 1$. Each coloured line corresponds to a parameter point labelled by a star of the same colour in figure 10. The cross-sections do not include ISR effects.

4.3 Summary of future collider prospects

We see that the flavonstrahlung cross-sections are likely too small for the process to be discovered at the HL-LHC, but a 100 TeV hadron collider and a 3 or 10 TeV muon collider could have excellent discovery prospects for multi-TeV mass flavons and Z' bosons. At a qualitative level, this is very similar to the pure Z' search prospects in the $B_3 - L_2$ model, as shown in ref. [21].

Comparing the 100 TeV hadron collider with the 10 TeV muon collider, we notice that for a given parameter space point, the flavonstrahlung cross-sections are two or three

JHEP03(2023)253

orders of magnitude greater at the muon collider. This is not surprising, considering that flavonstrahlung at a hadron collider occurs primarily through a bb partonic initial state, whereas the muon collider can harness almost the entire beam for the production of flavonstrahlung. The muon collider is limited by the kinematical threshold $m_\vartheta \lesssim 8\,\text{TeV}$ coming from the smaller beam energy, but even for the largest allowed couplings, the reach of the 100 TeV hadron collider is stopped in the same neighbourhood due to diminishing cross-sections.

To truly estimate discovery prospects, one of course should calculate backgrounds. However, it seems very likely that these can be controlled highly efficiently: with invariant mass cuts upon the reconstructed Z' from its decay products and also from the reconstructed flavon particle, from its decay products.

5 Conclusions

The $B_3 - L_2$ model is well motivated, being pertinent to the fermion mass puzzle[10] [1–3] as well as the $b \to s\mu^+\mu^-$ anomalies, and it is directly testable at colliders. Collider signatures remain currently relatively unstudied aside from a few Z' bump-hunts in di-fermion invariant masses. Even these had to be reinterpreted from the experimental papers because most interpretations of various bump-hunts in di-fermion invariant masses assumed family universality. The $B_3 - L_2$ model is far from the family universal limit; for studies of Z' production in the $B_3 - L_2$ model, see refs. [2, 3, 20, 21].

We have instead studied the prospects for flavonstrahlung, where the flavon is produced along with an associated Z'. Our results indicate that the flavon will not be directly discovered at the HL-LHC because its production cross-section is too small, but in a future 3 or 10 TeV muon collider or a 100 TeV FCC, flavonstrahlung discovery prospects are good. Flavons could also be produced at hadron colliders by traditional SM Higgs production processes, provided that they mix with the Higgs (i.e. provided that $\phi \neq 0$). Thus, they could be produced via gluon-gluon fusion, via weak boson fusion or via associated production with a di-top fermion. The advantage of the flavonstrahlung process is that it is present even in the limit of zero mixing with the SM Higgs field $\phi \to 0$. In fact, it becomes negligible for maximal mixing with the SM Higgs field, but the model must be far from this limit because of current bounds from Higgs measurements, as shown in figure 2.

Several other similar bottom-up models possess the flavonstrahlung signature, for example the Third Family Hypercharge Model [57] and its variants [58], gauged muon minus tau lepton number [59] and several other gauged $U(1)$ family non-universal models [60]. In the future, it may be of interest to compute the cross-sections for these models too in order to see how they compare.

One may ask what the first hints would be in collider data from beyond the SM effects of the $B_3 - L_2$ model. The answer, possibly, is the $b \to s\mu^+\mu^-$ anomalies that are currently being investigated [1–3]. One can also obtain deviations in M_W, as figure 2 implies. This figure also reminds us that (since we have applied the current bounds, the

[10] In particular, the model describes why the CKM quark mixing matrix elements $|V_{ub}| \ll 1$, $|V_{ts}| \ll 1$, $|V_{td}| \ll 1$ and $|V_{cb}| \ll 1$.

JHEP03(2023)253

sensitivity of which will increase with increased integrated luminosity) the LHC may also observe deviations from the SM limit in the signal strength of various Higgs cross-sections, should the flavon and Higgs fields mix. The first direct evidence for the model, however, would likely be from the classic $Z' \to \mu^+\mu^-$ resonance search, followed possibly by other Z' decay modes. Flavon particle production (via the usual Higgs production modes, but suppressed by powers of $\sin\phi$) could also be observed. Flavonstrahlung may eventually be observed at future colliders, with a resonant $\mu^+\mu^-$ produced in association with a flavon boson, which would primarily decay to W^+W^-, ZZ or HH, as displayed on figure 5.

Acknowledgments

This work has been partially supported by STFC consolidated grant ST/T000694/1. We thank the Cambridge Pheno Working Group for helpful discussions.

References

[1] R. Alonso, P. Cox, C. Han and T.T. Yanagida, *Flavoured $B-L$ local symmetry and anomalous rare B decays*, *Phys. Lett. B* **774** (2017) 643 [arXiv:1705.03858] [INSPIRE].

[2] C. Bonilla, T. Modak, R. Srivastava and J.W.F. Valle, *$U(1)_{B_3-3L_\mu}$ gauge symmetry as a simple description of $b \to s$ anomalies*, *Phys. Rev. D* **98** (2018) 095002 [arXiv:1705.00915] [INSPIRE].

[3] B.C. Allanach, *$U(1)_{B_3-L_2}$ explanation of the neutral current $B-$anomalies*, *Eur. Phys. J. C* **81** (2021) 56 [*Erratum ibid.* **81** (2021) 321] [arXiv:2009.02197] [INSPIRE].

[4] M. Algueró et al., *Emerging patterns of New Physics with and without Lepton Flavour Universal contributions*, *Eur. Phys. J. C* **79** (2019) 714 [*Addendum ibid.* **80** (2020) 511] [arXiv:1903.09578] [INSPIRE].

[5] A.K. Alok, A. Dighe, S. Gangal and D. Kumar, *Continuing search for new physics in $b \to s\mu\mu$ decays: two operators at a time*, *JHEP* **06** (2019) 089 [arXiv:1903.09617] [INSPIRE].

[6] M. Ciuchini et al., *New Physics in $b \to s\ell^+\ell^-$ confronts new data on Lepton Universality*, *Eur. Phys. J. C* **79** (2019) 719 [arXiv:1903.09632] [INSPIRE].

[7] J. Aebischer et al., *B-decay discrepancies after Moriond 2019*, *Eur. Phys. J. C* **80** (2020) 252 [arXiv:1903.10434] [INSPIRE].

[8] A. Datta, J. Kumar and D. London, *The B anomalies and new physics in $b \to se^+e^-$*, *Phys. Lett. B* **797** (2019) 134858 [arXiv:1903.10086] [INSPIRE].

[9] K. Kowalska, D. Kumar and E.M. Sessolo, *Implications for new physics in $b \to s\mu\mu$ transitions after recent measurements by Belle and LHCb*, *Eur. Phys. J. C* **79** (2019) 840 [arXiv:1903.10932] [INSPIRE].

JHEP03(2023)253

[10] A. Arbey et al., *Update on the b→s anomalies*, *Phys. Rev. D* **100** (2019) 015045 [arXiv:1904.08399] [INSPIRE].

[11] N. Gubernari, M. Reboud, D. van Dyk and J. Virto, *Improved theory predictions and global analysis of exclusive $b \to s\mu^+\mu^-$ processes*, *JHEP* **09** (2022) 133 [arXiv:2206.03797].

[12] A.K. Alok, N.R. Singh Chundawat, S. Gangal and D. Kumar, *A global analysis of $b \to s\ell\ell$ data in heavy and light Z' models*, *Eur. Phys. J. C* **82** (2022) 967 [arXiv:2203.13217] [INSPIRE].

[13] N.R. Singh Chundawat, *CP violation in $b \to s\ell\ell$: a model independent analysis*, arXiv:2207.10613 [INSPIRE].

[14] A.J. Buras and E. Venturini, *The exclusive vision of rare K and B decays and of the quark mixing in the standard model*, *Eur. Phys. J. C* **82** (2022) 615 [arXiv:2203.11960] [INSPIRE].

[15] A.J. Buras, *Standard Model predictions for rare K and B decays without new physics infection*, *Eur. Phys. J. C* **83** (2023) 66 [arXiv:2209.03968] [INSPIRE].

[16] LHCb collaboration, *Test of lepton universality in $b \to s\ell^+\ell^-$ decays*, arXiv:2212.09152 [INSPIRE].

[17] LHCb collaboration, *Measurement of lepton universality parameters in $B^+ \to K^+\ell^+\ell^-$ and $B^0 \to K^{*0}\ell^+\ell^-$ decays*, arXiv:2212.09153 [INSPIRE].

[18] J. Charles et al., *Future sensitivity to new physics in B_d, B_s, and K mixings*, *Phys. Rev. D* **89** (2014) 033016 [arXiv:1309.2293] [INSPIRE].

[19] M. Lim, F. Maltoni, G. Ridolfi and M. Ubiali, *Anatomy of double heavy-quark initiated processes*, *JHEP* **09** (2016) 132 [arXiv:1605.09411] [INSPIRE].

[20] B.C. Allanach, J.M. Butterworth and T. Corbett, *Large hadron collider constraints on some simple Z' models for $b \to s\mu^+\mu^-$ anomalies*, *Eur. Phys. J. C* **81** (2021) 1126 [arXiv:2110.13518] [INSPIRE].

[21] A. Azatov et al., *New physics in b b → sμμ: FCC-hh or a muon collider?*, *JHEP* **10** (2022) 149 [arXiv:2205.13552] [INSPIRE].

[22] ATLAS collaboration, *Search for high-mass dilepton resonances using 139 fb^{-1} of pp collision data collected at $\sqrt{s}$ =13 TeV with the ATLAS detector*, *Phys. Lett. B* **796** (2019) 68 [arXiv:1903.06248] [INSPIRE].

[23] CMS collaboration, *Search for resonant and nonresonant new phenomena in high-mass dilepton final states at $\sqrt{s}$ = 13 TeV*, *JHEP* **07** (2021) 208 [arXiv:2103.02708] [INSPIRE].

[24] Muon Collider collaboration, *A Muon Collider Facility for Physics Discovery*, arXiv:2203.08033 [INSPIRE].

[25] FCC collaboration, *FCC-hh: The Hadron Collider: Future Circular Collider Conceptual Design Report Volume 3*, *Eur. Phys. J. ST* **228** (2019) 755 [INSPIRE].

[26] G.M. Pruna, *Phenomenology of the minimal $B - L$ Model: the Higgs sector at the Large Hadron Collider and future Linear Colliders*, Ph.D. thesis, Southampton University (2011) [arXiv:1106.4691] [INSPIRE].

[27] S. Banerjee, M. Mitra and M. Spannowsky, *Searching for a Heavy Higgs boson in a Higgs-portal B-L Model*, *Phys. Rev. D* **92** (2015) 055013 [arXiv:1506.06415] [INSPIRE].

[28] B. Kors and P. Nath, *Aspects of the Stueckelberg extension*, *JHEP* **07** (2005) 069 [hep-ph/0503208] [INSPIRE].

JHEP03(2023)253

[29] C.D. Froggatt and H.B. Nielsen, *Hierarchy of Quark Masses, Cabibbo Angles and CP Violation*, *Nucl. Phys. B* **147** (1979) 277 [INSPIRE].

[30] R. Bause et al., *B-anomalies from flavorful U(1)′ extensions, safely*, *Eur. Phys. J. C* **82** (2022) 42 [arXiv:2109.06201] [INSPIRE].

[31] V. Barger et al., *Complex Singlet Extension of the Standard Model*, *Phys. Rev. D* **79** (2009) 015018 [arXiv:0811.0393] [INSPIRE].

[32] G.M. Pruna and T. Robens, *Higgs singlet extension parameter space in the light of the LHC discovery*, *Phys. Rev. D* **88** (2013) 115012 [arXiv:1303.1150] [INSPIRE].

[33] A. Falkowski, C. Gross and O. Lebedev, *A second Higgs from the Higgs portal*, *JHEP* **05** (2015) 057 [arXiv:1502.01361] [INSPIRE].

[34] A. Alloul et al., *FeynRules 2.0 - A complete toolbox for tree-level phenomenology*, *Comput. Phys. Commun.* **185** (2014) 2250 [arXiv:1310.1921] [INSPIRE].

[35] C. Degrande et al., *UFO - The Universal FeynRules Output*, *Comput. Phys. Commun.* **183** (2012) 1201 [arXiv:1108.2040] [INSPIRE].

[36] W. Altmannshofer and P. Stangl, *New physics in rare B decays after Moriond 2021*, *Eur. Phys. J. C* **81** (2021) 952 [arXiv:2103.13370] [INSPIRE].

[37] M. Ciuchini et al., *Constraints on lepton universality violation from rare B decays*, *Phys. Rev. D* **107** (2023) 055036 [arXiv:2212.10516] [INSPIRE].

[38] T. Robens and T. Stefaniak, *Status of the Higgs Singlet Extension of the Standard Model after LHC Run 1*, *Eur. Phys. J. C* **75** (2015) 104 [arXiv:1501.02234] [INSPIRE].

[39] T. Robens, *Constraining extended scalar sectors at current and future colliders - an update*, in the proceedings of the *8th Workshop on Theory, Phenomenology and Experiments in Flavour Physics: Neutrinos, Flavor Physics and Beyond*, (2022) [arXiv:2209.15544] [INSPIRE].

[40] Particle Data Group collaboration, *Review of Particle Physics*, *PTEP* **2022** (2022) 083C01 [INSPIRE].

[41] P. Bechtle et al., *Recent Developments in HiggsBounds and a Preview of HiggsSignals*, *PoS* **CHARGED2012** (2012) 024 [arXiv:1301.2345] [INSPIRE].

[42] P. Bechtle et al., HiggsBounds – 4*: Improved Tests of Extended Higgs Sectors against Exclusion Bounds from LEP, the Tevatron and the LHC*, *Eur. Phys. J. C* **74** (2014) 2693 [arXiv:1311.0055] [INSPIRE].

[43] P. Bechtle et al., *HiggsBounds: Confronting Arbitrary Higgs Sectors with Exclusion Bounds from LEP and the Tevatron*, *Comput. Phys. Commun.* **181** (2010) 138 [arXiv:0811.4169] [INSPIRE].

[44] P. Bechtle et al., *HiggsBounds 2.0.0: Confronting Neutral and Charged Higgs Sector Predictions with Exclusion Bounds from LEP and the Tevatron*, *Comput. Phys. Commun.* **182** (2011) 2605 [arXiv:1102.1898] [INSPIRE].

[45] P. Bechtle et al., *HiggsBounds-5: Testing Higgs Sectors in the LHC 13 TeV Era*, *Eur. Phys. J. C* **80** (2020) 1211 [arXiv:2006.06007] [INSPIRE].

[46] P. Bechtle et al., *Applying Exclusion Likelihoods from LHC Searches to Extended Higgs Sectors*, *Eur. Phys. J. C* **75** (2015) 421 [arXiv:1507.06706] [INSPIRE].

JHEP03(2023)253

[47] D. López-Val and T. Robens, *Δr and the W-boson mass in the singlet extension of the standard model*, *Phys. Rev. D* **90** (2014) 114018 [arXiv:1406.1043] [INSPIRE].

[48] A. Sirlin, *Radiative Corrections in the SU(2)-L x U(1) Theory: A Simple Renormalization Framework*, *Phys. Rev. D* **22** (1980) 971 [INSPIRE].

[49] W.F.L. Hollik, *Radiative Corrections in the Standard Model and their Role for Precision Tests of the Electroweak Theory*, *Fortsch. Phys.* **38** (1990) 165 [INSPIRE].

[50] A. Denner, *Techniques for calculation of electroweak radiative corrections at the one loop level and results for W physics at LEP-200*, *Fortsch. Phys.* **41** (1993) 307 [arXiv:0709.1075] [INSPIRE].

[51] J.D. Wells, *TASI lecture notes: Introduction to precision electroweak analysis*, in the proceedings of the *Theoretical Advanced Study Institute in Elementary Particle Physics: Physics in $D \geqq 4$*, (2005), pp. 41–64 [hep-ph/0512342] [INSPIRE].

[52] T. Hahn, *Generating Feynman diagrams and amplitudes with FeynArts 3*, *Comput. Phys. Commun.* **140** (2001) 418 [hep-ph/0012260] [INSPIRE].

[53] T. Hahn and M. Perez-Victoria, *Automatized one loop calculations in four-dimensions and D-dimensions*, *Comput. Phys. Commun.* **118** (1999) 153 [hep-ph/9807565] [INSPIRE].

[54] J. Alwall et al., *Computing decay rates for new physics theories with FeynRules and MadGraph 5_aMC@NLO*, *Comput. Phys. Commun.* **197** (2015) 312 [arXiv:1402.1178] [INSPIRE].

[55] J. Alwall et al., *The automated computation of tree-level and next-to-leading order differential cross sections, and their matching to parton shower simulations*, *JHEP* **07** (2014) 079 [arXiv:1405.0301] [INSPIRE].

[56] Y. Bao, J.J. Fan and L. Li, *Electroweak ALP searches at a muon collider*, *JHEP* **08** (2022) 276 [arXiv:2203.04328] [INSPIRE].

[57] B.C. Allanach and J. Davighi, *Third family hypercharge model for $R_{K^{(*)}}$ and aspects of the fermion mass problem*, *JHEP* **12** (2018) 075 [arXiv:1809.01158] [INSPIRE].

[58] B.C. Allanach and J. Davighi, *Naturalising the third family hypercharge model for neutral current B-anomalies*, *Eur. Phys. J. C* **79** (2019) 908 [arXiv:1905.10327] [INSPIRE].

[59] X.G. He, G.C. Joshi, H. Lew and R.R. Volkas, *New Z' phenomenology*, *Phys. Rev. D* **43** (1991) 22 [INSPIRE].

[60] A. Greljo et al., *Muonic force behind flavor anomalies*, *JHEP* **04** (2022) 151 [arXiv:2107.07518] [INSPIRE].

JHEP03(2023)253